Cooperation of ultrathin bowl-shaped scaffolds and oxygen vacancies promoting selective photo-oxidation of aromatic alcohols on layered oxyhalide PbBiO$_2$Cl

Danjun Mao [a,1], Tong Li [a,1], Huan He [b,*], Shuxue Yang [a], Shaogui Yang [b], Cheng Sun [a], Shourong Zheng [a], Zhifeng Jiang [c,d], Zhaoyi Xu [a,*], Po Keung Wong [c], Xiaolei Qu [a,*]

[a] State Key Laboratory of Pollution Control and Resource Reuse, School of the Environment, Nanjing University, Nanjing 210023, China
[b] School of Environment, Nanjing Normal University, Nanjing 210023, China
[c] School of Life Sciences, The Chinese University of Hong Kong, Shatin, NT 999077, Hong Kong Special Administrative Region of China
[d] Institute for Energy Research, Jiangsu University, 301 Xuefu Road, Zhenjiang 212013, China

ARTICLE INFO

ABSTRACT

Photocatalytic selective oxidation of aromatic alcohols into value-added chemicals has attracted increasing attention. Yet most processes suffer from sluggish charge kinetics, weak O$_2$ affinity, low conversion efficiency and selectivity, which restrict their practical development. Herein, PbBiO$_2$Cl ultrathin bowls (UBs) with rich oxygen vacancies (R$_{OV}$) were initially fabricated via a combined microemulsion method and in-situ reduction process. The ultrathin bowl-shaped geometry and rich OVs effectively boost light absorption and charge separation. Theoretical results indicate the OVs on PbBiO$_2$Cl not only generate abundant localized electrons, but also afford strong interfacial covalent bonds between O$_2$ and OVs, which can act as atomic-level electron transfer highway and effectively promote the O$_2$ adsorption and activation. As a result, R$_{OV}$-PbBiO$_2$Cl UBs show a 5.2-fold enhanced activity for aerobic oxidation of alcohols to aldehydes relative to PbBiO$_2$Cl nanoplates (NPs). This work may inspire the design of more open hollow scaffolds with defect engineering for artificial photosynthesis.

1. Introduction

Valorization of the carbonyl group, a versatile structural motif in various chemical compounds, plays a crucial role in synthetic chemistry and carbon feedstock manufacturing [1–3]. This typically involves selective oxidation from aromatic alcohols to the corresponding aldehydes or ketones, which are the indispensable building blocks for the fabrication of high-value-added chemicals [4–6]. Unfortunately, conventional methods for alcohol oxidation often involve harsh reaction conditions and strong oxidizing agents, which inevitably render undesired energy consumption and negative environmental impacts [7–9]. In contrast, photocatalytic organic conversion holds great promise in the manufacture of value-added carbonyl compounds as it can be conducted under mild conditions using clean and inexhaustible solar energy [10–13]. However, the progress still undergoes low photoconversion rate and limited selectivity. In this regard, the exploration of efficient and selective valorization of aromatic alcohols to target products under ambient temperature and pressure is highly demanded.

Recently, several encouraging strategies including defect engineering and morphological nanostructures have been investigated and showed outstanding potentials for various solar-related applications [14–16]. The introduction of surface oxygen vacancies (OVs) can form rich localized charges during the neighboring metal sites. These asymmetric charge distributions generate locally polarized electric field, which facilitates the effective transfer of the trapped interfacial charge to the adsorbate [17]. Meanwhile, the OVs could afford abundant co-ordination unsaturated surface atoms, which can act as catalytic active sites for promoting the subsequent interfacial redox reactions [18]. Moreover, the presence of OVs can effectively activate molecular oxygen to produce highly reactive oxygen species (ROS), which is particularly important for the O$_2$-involved organic transformations.

As a Sillén-structured single metal oxyhalide, BiOX (X = Cl, Br, I) has received significant attention in photocatalytic oxidative organic synthesis due to the unique layered structure and favorable band-edge

---

potentials [19–22]. However, compared with the widely reported single metal oxyhalide photocatalysts, bimetallic oxyhalides, such as $PbBiO_2X$ (X = Cl, Br, I), are rarely explored for selective photo-oxidative organic synthesis because of the high recombination of electron-hole pairs and weak O_2 adsorption. As we known, hollow bowl-shaped structure with ultrathin-shelled topologies could effectively promote charge separation due to the reduced diffusion resistance and boosted light-harvesting by elongated light scattering [23,24]. Nevertheless, due to the restricted crystal growth conditions, the controlled synthesis of bimetallic oxyhalides with the desired hollow bowl-shaped scaffolds still requires further exploration. Therefore, the design of bimetallic oxyhalides with ultrathin bowl-shaped structures and rich oxygen vacancies to achieve more effective charge separation and O_2 activation is extremely attractive, but rarely achieved.

To prove the above considerations, the hollow bowl-shaped $PbBiO_2Cl$ structure with ultrathin-shelled topologies and rich oxygen vacancies was designed and synthesized for the first time via a combined ionic liquid-in-water (IL/W) microemulsion process and in-situ reduction method. The bowl-shaped scaffolds with ultrathin-shelled topologies are able to adequately suppress bulk recombination of electron-hole pairs owing to the reduced carrier diffusion resistance. The introduction of OVs on the surface of $PbBiO_2Cl$ not only broadens the photo-absorption and enhances charge separation, but also causes an asymmetric distribution of charge and affords rich localized electrons, effectively promoting the molecular oxygen adsorption and activation. Expectedly, the bowl-shaped $PbBiO_2Cl$ with rich OVs (R_{OV}-$PbBiO_2Cl$ UBs) shows significantly improved photocatalytic activity for selective valorization of aromatic alcohols to aldehydes (Con. 94 %, Sel. **> 99 %**), which is 5.2 times higher than that of $PbBiO_2Cl$ nanoplates counterpart ($PbBiO_2Cl$ NPs, Con. 18 %, Sel. **> 99 %**). Besides, the in-depth and atomic insight mechanisms of the bowl-shaped structures with rich oxygen vacancies were further uncovered by comprehensively experimental and theoretical results.

2. Experimental section

2.1. Synthesis of ultrathin bowl-shaped $PbBiO_2Cl$ with different oxygen vacancy concentrations

In a typical experiment, 1 mmol 1-octyl-3-methylimidazolium chloride (OmimCl) as the oil-phase and 0.2 g TX-100 as the stabilizer were dissolved in 25 mL deionized water under vigorous stirring for 1 h to form the underlying IL/W microemulsion. 1 mmol $Bi(NO_3)_3 \cdot 5 H_2O$ and 1 mmol $Pb(NO_3)_2$ were added into 5 mL HNO_3 solution (1 M) to form a homogeneous solution, which was then added dropwise into the above IL/W microemulsion system with continuous stirring. Subsequently, a certain amount of glyoxal (0, 0.1 and 0.2 mL) was added into the mixed solution and the pH value was adjusted to 10 with 2 M NaOH. After stirring at room temperature for 30 min, the mixture was transferred into a 50 mL Teflon-lined autoclave, sealed and heated at 120 °C for 6 h. Afterwards, the samples were collected, thoroughly washed with ethanol and deionized water for many times, and then dried overnight under vacuum at 60 °C for further characterization. The obtained products are designated as $PbBiO_2Cl$ UBs, P_{OV}-$PbBiO_2Cl$ UBs ($PbBiO_2Cl$ UBs with poor oxygen vacancies) and R_{OV}-$PbBiO_2Cl$ UBs, respectively.

2.2. Synthesis of $PbBiO_2Cl$ nanoplates

Typically, 1 mmol $Bi(NO_3)_3 \cdot 5 H_2O$, 1 mmol $Pb(NO_3)_2$ and 1 mmol OmimCl were added into 25 mL deionized water and stirred for 30 min at room temperature. The pH value of the above suspension was adjusted to 10 with 2 M NaOH under continuous stirring. Subsequently, the mixture was added into 50 mL autoclave for the hydrothermal treatment at 160 °C for 6 h. The resulting precipitate was collected, consecutively washed with absolute ethanol and deionized water, and then dried overnight under vacuum at 60 °C for further characterization.

2.3. Characterization

The phases of the series of $PbBiO_2Cl$ materials were verified by X-ray powder diffraction (XRD) on a Bruker D8-advance X-ray diffractometer equipped with monochromatized Cu Kα radiation (λ = 1.5406 Å). The morphology and atomic structure of the $PbBiO_2Cl$ photocatalysts were characterized by scanning electron microscope (SEM, QUANTA FEG 250, USA), transmission electron microscopy (TEM) and aberration-corrected scanning transmission electron microscopy with high-angle annular dark-field (HAADF-STEM, FEI TF20). The surface atomic oxidation state of $PbBiO_2Cl$ was analyzed by X-ray photoelectron spectroscopy (XPS) on a PHI5000 Versa Probe electron spectrometer with an excitation source of Al Kα (ULVAC-PHI, Japan). The atomic coordination environment and electron spin conformation were surveyed by electron paramagnetic resonance (EPR) spectroscopy on a Bruker model ESR JES-FA200 spectrometer at room temperature. BET specific surface areas of the products were tested on a Micromeritics ASAP 2020 apparatus. The light absorption properties of the $PbBiO_2Cl$ samples was determined by the UV–vis diffuse reflectance spectroscopy (DRS) on a UV-3600 spectrophotometer (Shimadzu, Japan). The fluorescence lifetime was collected on a QuantaMaster and TimeMaster Spectrofluorometer (QuantaMastertTM40, USA). In situ Fourier-transform infrared (FTIR) spectra were recorded using a Thermo Scientific Nicolet iS10 instrument with an in-situ Harrick IR cell.

2.4. Photoelectrochemical measurements

Photocurrent response and electrochemical impedance spectroscopy (EIS) experiments were conducted using a CHI-760E electrochemical workstation (Chenhua Apparatus Corporation, China) in a standard three-electrode system, with a commercial Ag/AgCl electrode serving as the reference electrode and a platinum wire as the counter electrode. Working electrodes were prepared by dispersing 20 mg of the catalysts in 3 mL of ethanol by sonication for 5 h to form a homogeneous colloidal solution. The resulting colloid was then dropwise added onto a previously treated ITO slice (1.0×1.0 cm^{-2}) and dried at 60 °C in air for 6 h. The electrolyte used was a 0.1 M Na_2SO_4 solution and simulated solar light was generated using a 300 W Xenon lamp. EIS data was recorded at the open-circuit potential with a frequency range from 10^6 to 10 Hz. The photocurrent measurements were conducted using the amperometric i-t curve mode with a 0.6 V bias voltage for 600 s

2.5. Photocatalytic aerobic oxidation of aromatic alcohols

The photocatalytic aerobic oxidation of aromatic alcohols was carried out in a 25 mL side-irradiation quartz reactor with continuous stirring. Typically, 50 mg of photocatalyst was placed into 10 mL of 5 mmol·L^{-1} aromatic alcohol n-hexane solution, which was then bubbled with O_2 for 30 min. Then, the reactor was sealed and irradiated by a 300 W xenon lamp with a 400 nm cut-off filter (PLS-SXE300UV, Beijing Perfectlight Technology Co., Ltd., China). The reaction temperature was controlled at 298 K by a recirculating cooling water system during irradiation (DC-0506, Shanghai Sunny Hengping Scientific Instrument Co., Ltd., China). After irradiation for 8 h, the liquid products were analyzed by gas chromatography (7890B, Agilent) equipped with Flame Ionization Detector (FID). To detect the active species, 10 mM of various trapping agents including isopropanol (IPA), carbon tetrachloride (CCl_4), triethanolamine (TEOA), butylated hydroxytoluene (BHT) and p-benzoquinone (p-BQ) were employed as the scavengers for hydroxyl radicals (•OH), electrons (e$^-$), holes (h$^+$), carbon centered radicals (•C) and superoxide radicals (•O_2^-), respectively.

2.6. Theoretical calculations

All the simulation calculations of structure relaxation, charge density difference, single-point energies and O_2 adsorption energy were

investigated in the Vienna ab initio simulation package (VASP) code. The projector augmented wave (PAW) method was chosen to describe the ion-electron interactions in PbBiO$_2$Cl, and the exchange and correlations were handled by the Generalized gradient approximation (GGA) using Perdew-Burke-Ernzerhof (PBE) formulation. All-electron plane-wave basis sets with a kinetic energy cutoff of 400 eV were employed. The conventional energy threshold of 10^{-5} eV and force convergence criteria of 0.02 eV/Å was adapted to realize ionic relaxations. The equilibrium lattice constants of orthorhombic PbBiO$_2$Cl unit cell were optimized, when using a $2 \times 2 \times 3$ Monkhorst-Pack k-point grid for

Brillouin zone sampling, to be a= 5.641 Å, b= 5.596 Å, c= 12.156 Å.

The isosurface of the charge density difference was defined as followed:

$$\Delta\rho\,(r) = \rho_{ov\text{-}sur}\,(r) - \rho_{sur}\,(r)$$

where the $\Delta\rho\,(r)$ is the charge difference between $\rho_{ov\text{-}sur}\,(r)$ and $\rho_{sur}\,(r)$.

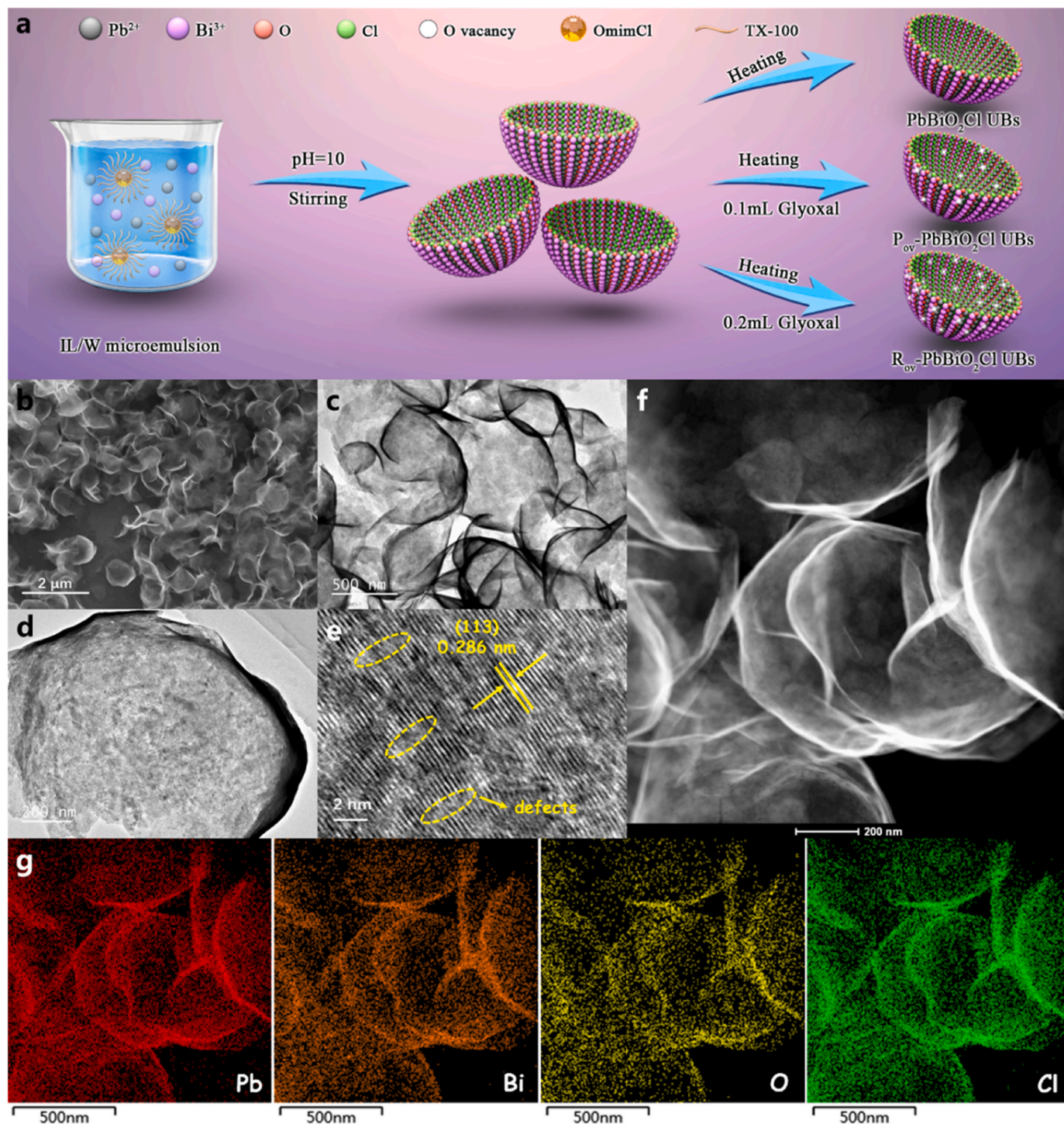The adsorption energy (E_{ads}) for O$_2$ molecules was calculated as follows:

Fig. 1. (a) SEM image, (b-c) TEM images, (d) HRTEM image, (e) HADDF-STEM image and (f) HADDF-STEM-EDS mapping of Pb, Bi, O, Cl elements over the R$_{OV}$-PbBiO$_2$Cl UBs.

$$E_{ads} = E_{tot} - (E_{sur} + E_{mol})$$

Here, E_{tot} represents the total energies of the adsorption system, E_{sur} shows the energy of pure surface and E_{mol} refers to the energy of isolated molecule.

3. Results and discussion

3.1. Structure and morphology analysis

PbBiO$_2$Cl ultrathin bowls were initially fabricated via a versatile ionic liquid-in-water (IL/W) microemulsion process (Fig. 1a). The surfactant TX-100 serves as the structural stabilizer at the interface between OmimCl and water in the ternary microemulsion, which is crucial to the formation of the hollow bowl-shaped structure [25]. Owing to the limited miscibility of the OmimCl with water, susceptible and unstable emulsion droplets are formed under vigorous stirring [26]. As shown in Fig. S1, only PbBiO$_2$Cl NPs were obtained by using the same procedure as PbBiO$_2$Cl UBs without adding TX-100. Upon the addition of TX-100, stable OmimCl/TX-100/water ternary microemulsions were obtained, which can be ascribed to the hydrophobic effect and hydrogen bond formation between the OmimCl and TX-100. Subsequently, upon gradually introducing Bi^{3+} and Pb^{2+} ions into the ternary system, they will react with OmimCl at the interface to form hollow structures, which might crack and fragment owing to the thin shells. However, the exact growth mechanism still needs further exploration. Moreover, due to the reducibility of glyoxal, Pb^{2+} and Bi^{3+} could be partially reduced by the electrons of glyoxal under hydrothermal process, leading to the escape of neighboring oxygen atoms and ultimately forming defect structures [27]. The X-ray diffraction (XRD) pattern was used to confirm the formation of PbBiO$_2$Cl. As shown in Fig. S2, the characteristic diffraction peaks of all the PbBiO$_2$Cl NPs and UBs samples can be readily indexed to the orthorhombic phase of PbBiO$_2$Cl (JCPDS Card No. 13–0352), indicating the presence of OVs does not alter the crystalline phase of the photocatalysts.

The morphology and microstructure of as-obtained PbBiO$_2$Cl samples in the ternary microemulsion were analyzed by scanning electron microscopy (SEM), transmission electron microscope (TEM) and atomic resolution high-angle annular dark-field scanning TEM (HAADF-STEM). It can be clearly seen that the products obtained in the ternary microemulsion exhibit a uniform hollow bowl-shaped structure with distinct dark edges and bright interiors (Fig. 1b-f and Fig. S3a-d). The diameters of the ultrathin bowls range from 800 to 1000 nm, the thickness of the ultrathin bowls is approximately 5.0 nm, and the specific surface area is about 30–32 m^2/g for the three ultrathin bowl-shaped samples (Fig. S4). These results further indicate that the OV creation by glyoxal does not change the microstructure of PbBiO$_2$Cl UBs. In contrast to the neat and clear lattice stripes of PbBiO$_2$Cl UBs (Fig. S3d), some fuzzy and disordered regions of the atomic lattice were observed on the R$_{OV}$-PbBiO$_2$Cl UBs (Fig. 1e), which could be ascribed to surface unsaturated coordination induced by the escape of oxygen atoms as the formation of OVs on the PbBiO$_2$Cl UBs [28]. The HADDF-STEM-EDS elemental mapping suggests the even distribution of Pb, Bi, O, and Cl across the R$_{OV}$-PbBiO$_2$Cl UBs (Fig. 1g).

To confirm the atomic coordination environment and electron spin conformation changes in the PbBiO$_2$Cl NPs and UBs, electron paramagnetic resonance (EPR) spectroscopy was surveyed. In contrast to PbBiO$_2$Cl NPs and PbBiO$_2$Cl UBs, the characteristic signal at g = 2.001 was observed for P$_{OV}$-PbBiO$_2$Cl UBs and R$_{OV}$-PbBiO$_2$Cl UBs, which can be ascribed to the electrons trapped in OVs (Fig. 2a) [29,30]. The gradually intensified EPR signal from P$_{OV}$-PbBiO$_2$Cl UBs to R$_{OV}$-PbBiO$_2$Cl UBs evidences the increase of OVs concentration. X-ray photoelectron spectra (XPS) were then obtained to illustrate the surface atomic oxidation state changes in the PbBiO$_2$Cl NPs and UBs samples. The full survey spectra of the PbBiO$_2$Cl samples showed four constituent elements of Pb, Bi, O, and Cl elements (Fig. S5). Compared with PbBiO$_2$Cl NPs and PbBiO$_2$Cl UBs, an evident shift to lower binding energies for the P$_{OV}$-PbBiO$_2$Cl UBs and R$_{OV}$-PbBiO$_2$Cl UBs is observed in the high-resolution Bi 4 f and Pb 4 f core spectra (Fig. 2b,c). This downshift which compensates the charge nonequilibrium illustrates the decrease in the coordination number of Bi^{3+} and Pb^{2+} of the defective PbBiO$_2$Cl UBs [31]. Additionally, the appearance of lower valence states Bi$^{(3-x)+}$ and Pb$^{(2-x)+}$ also indicated the increase of OVs [32]. Besides,
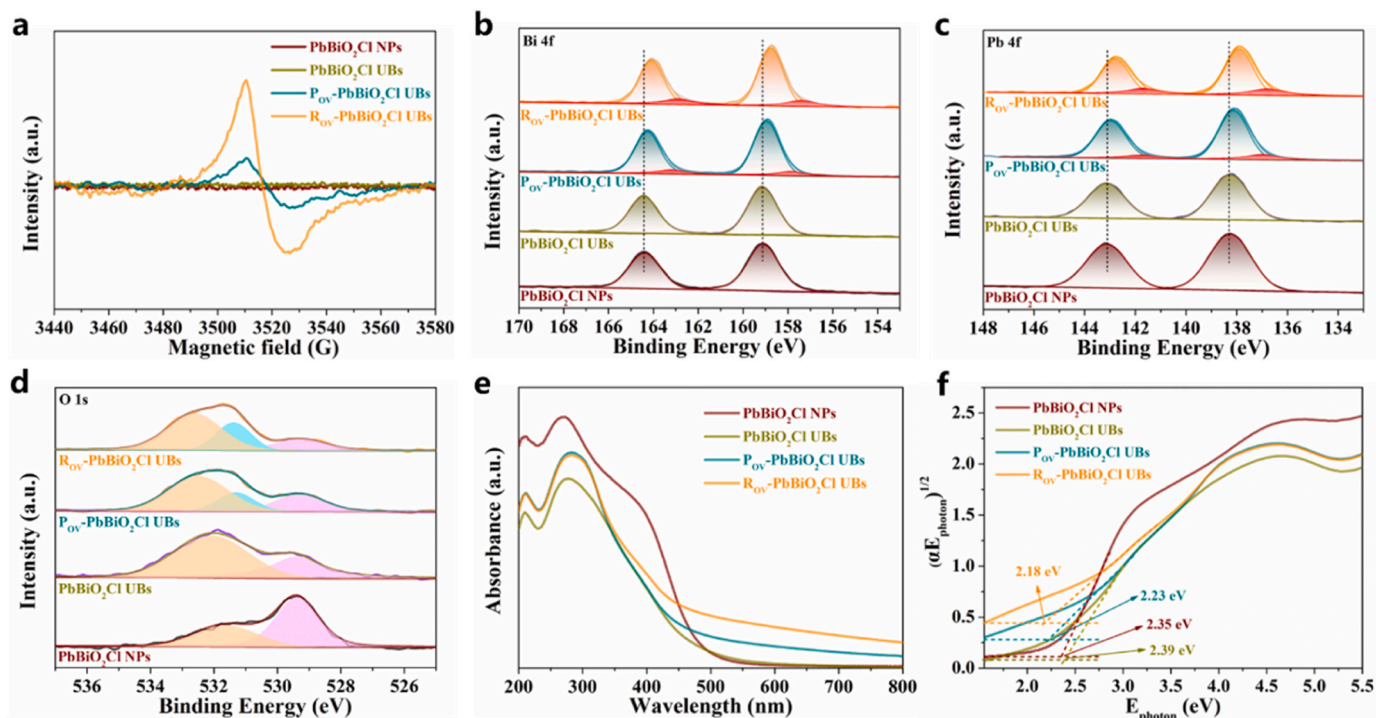

Fig. 2. (a) EPR spectra, (b) Bi 4 f, (c) Pb 4 f, (d) O 1 s XPS spectra, (e) DRS spectra and (f) tauc plots of the PbBiO$_2$Cl NPs, PbBiO$_2$Cl UBs, P$_{OV}$-PbBiO$_2$Cl UBs and R$_{OV}$-PbBiO$_2$Cl UBs.

the high-resolution XPS spectra of O 1 s shown in Fig. 2d disclose the existence of lattice oxygens and surface hydroxy groups for all the PbBiO$_2$Cl samples. Note that a new peak at 531.2 eV appears in P$_{OV}$-PbBiO$_2$Cl UBs and R$_{OV}$-PbBiO$_2$Cl UBs, which can be attributed to the oxygen atoms in the vicinity of an oxygen vacancy [33,34]. The higher oxygen vacancy concentration can be observed in R$_{OV}$-PbBiO$_2$Cl UBs relative to P$_{OV}$-PbBiO$_2$Cl UBs, indicating that the concentration of OVs can be effectively regulated by glyoxal, in agreement with the above EPR results.

Moreover, to obtain more information about the intrinsic nature of the as-synthesized PbBiO$_2$Cl samples, UV–vis diffuse reflectance spectrum was recorded (Fig. 2e). Compared with PbBiO$_2$Cl NPs, the absorption edge of PbBiO$_2$Cl UBs displays a significant blue shift, which can be ascribed to quantum confinement effect caused by the formation of ultrathin structure, similar phenomenon has been observed in previous literatures [35]. Contrastingly, with the introduction of OVs, the photo-absorption range of the defective PbBiO$_2$Cl UBs is significantly extended to 800 nm, the absorption capacity of the products is gradually increased from P$_{OV}$-PbBiO$_2$Cl UBs to R$_{OV}$-PbBiO$_2$Cl UBs, which is ascribed to the increase of OVs concentration. The corresponding band gap of PbBiO$_2$Cl NPs, PbBiO$_2$Cl UBs, P$_{OV}$-PbBiO$_2$Cl UBs and R$_{OV}$-PbBiO$_2$Cl UBs are calculated to be 2.35, 2.39, 2.23 and 2.18 eV by the Kubelka-Munk equation, respectively (Fig. 2f). In combination with the valence band (VB) XPS spectra (Fig. S6), the conduction band (CB) positions of PbBiO$_2$Cl NPs, PbBiO$_2$Cl UBs, P$_{OV}$-PbBiO$_2$Cl UBs and R$_{OV}$-PbBiO$_2$Cl UBs are estimated to be -0.51, -0.53, -0.56 and -0.58 eV, respectively, all the PbBiO$_2$Cl samples possessing the thermodynamic feasibility for O$_2$ reduction to·O$_2^-$ (Fig. S7).

To further reveal the effect of oxygen vacancies on the electronic properties of PbBiO$_2$Cl, density-functional-theory (DFT) calculation was thereby calculated. As displayed in Fig. 3a-b, the projected density of states (PDOS) of the oxygen-defective PbBiO$_2$Cl slab introduced a shallow donor state at the conduction-band edge relative to the pristine PbBiO$_2$Cl slab. The donor state mainly composed of the Bi 6p and Pb 6p orbitals may decrease the intrinsic bandgap of PbBiO$_2$Cl, which was beneficial to enhance the photo-absorption and promote the charge separation efficiency [31,36]. Moreover, as shown by the charge density difference in Fig. 3c,d, the electrons around the OVs tended to accumulate on the adjacent Bi and Pb atoms. Bader charge calculation further demonstrated that oxygen vacancies donated electrons to the adjacent metal atoms (Fig. 3e), leading to the formation of abundant electronic-rich active sites, which facilitates the adsorption of O$_2$ and subsequently transfer to the anti-bonding orbitals of the absorbed O$_2$, thus effectively promoting O$_2$ activation [37–39]. Based on the above collective results, it is highly desirable to fabricate hollow bowl-shaped structures with ultrathin-shelled topologies and abundant oxygen vacancies for the O$_2$-involved organic transformations.

3.2. Photocatalytic performance for selective oxidation of aromatic alcohol

To unveil how the hollow bowl-shaped scaffolds and abundant oxygen vacancies affect the photocatalytic activity of as-synthesized PbBiO$_2$Cl samples, selective valorization of benzyl alcohol into benzaldehyde using O$_2$ as a green oxidant was first estimated. Fig. 4a compares the relative performance of the four PbBiO$_2$Cl samples. With no change to their relative selectivity (> 99 %), the benzyl alcohol conversion efficiency was increased from the PbBiO$_2$Cl NPs (18 %) to the PbBiO$_2$Cl UBs (52 %) with the fabrication of ultrathin bowl-shaped structure, which could effectively promote charge separation due to the reduced diffusion resistance and boosted light-harvesting by elongated light scattering. Noticeably, the conversion of benzyl alcohol is further
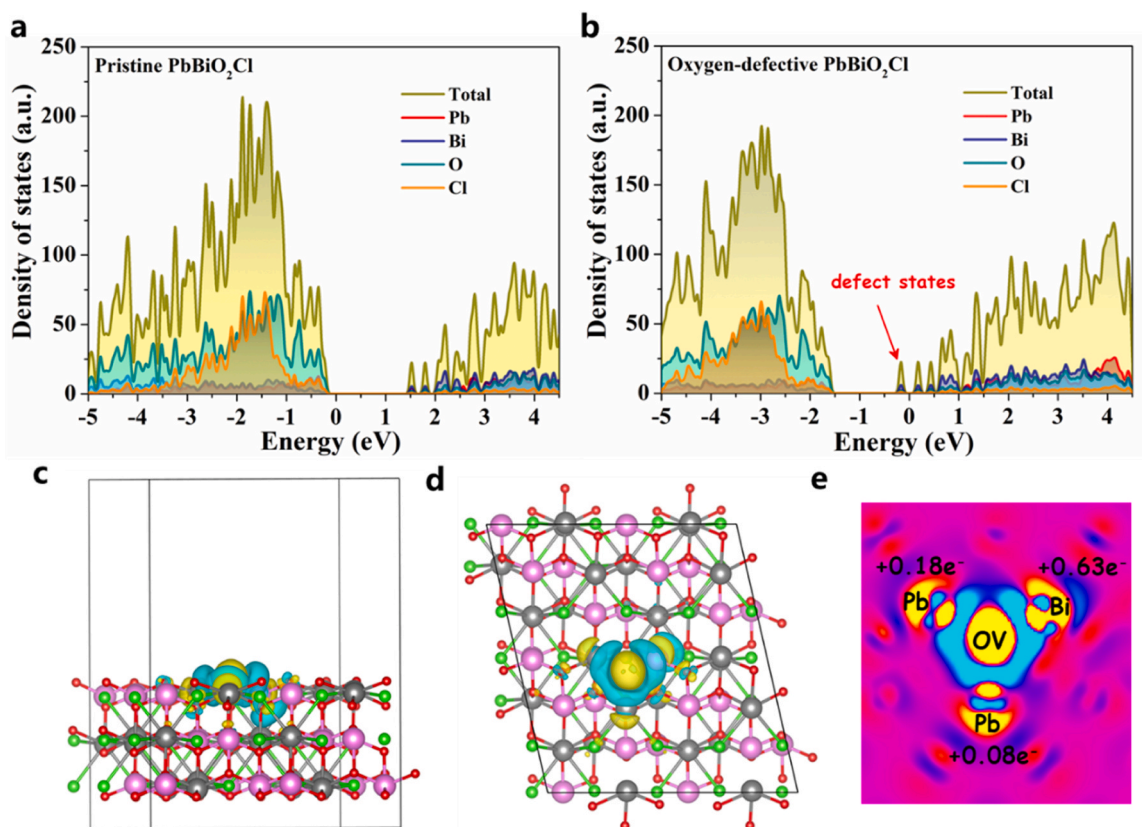

Fig. 3. (a-b) Calculated projected densities of states (PDOS) of pristine and oxygen-defective PbBiO$_2$Cl; (c-d) Three-dimensional and (e) two-dimensional images of the difference charge density contour plots of oxygen defective PbBiO$_2$Cl (isosurface set at 0.0015e Å^{-3}); the yellow and blue regions indicate electron accumulation and depletion, respectively.
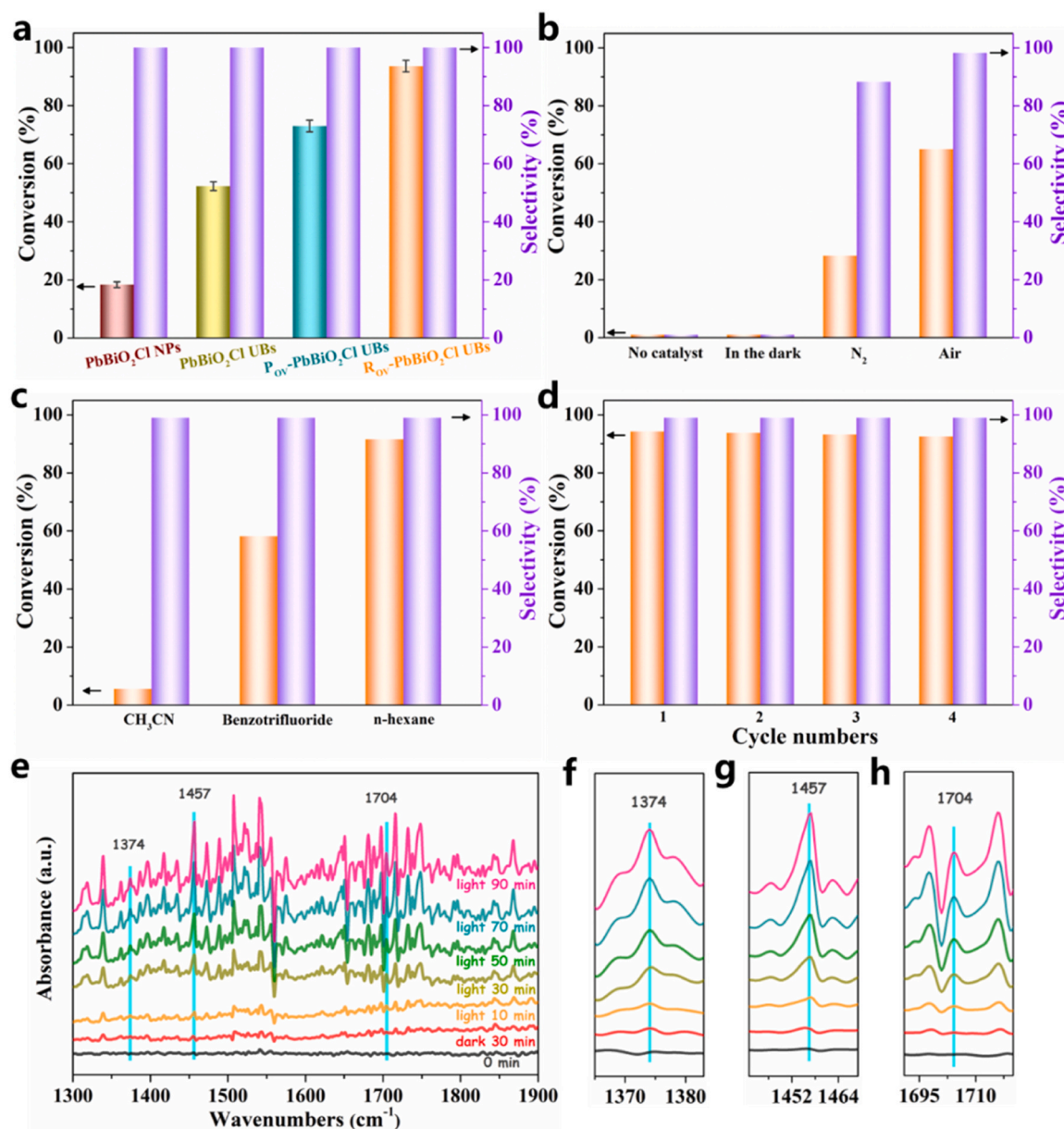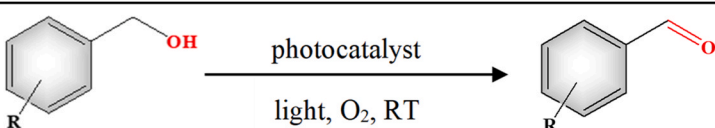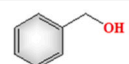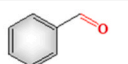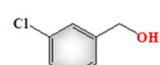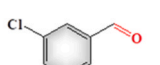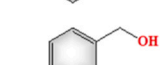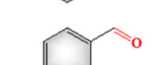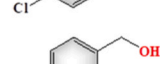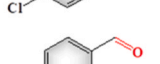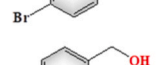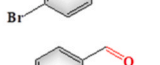
Fig. 4. (a) Photocatalytic aerobic oxidation of benzyl alcohol over the as-prepared PbBiO$_2$Cl NPs and UBs under light irradiation. (b-c) Control experiment and (d) recycling tests over R$_{OV}$-PbBiO$_2$Cl UBs. (e-h) Time-dependent in situ FTIR spectra of the benzyl alcohol evolution over the R$_{OV}$-PbBiO$_2$Cl UBs.

enhanced by the introduction of OVs. R$_{OV}$-PbBiO$_2$Cl UBs and P$_{OV}$-PbBiO$_2$Cl UBs could achieve 94 % and 73 % conversion ratio, respectively, which were much better than those of PbBiO$_2$Cl UBs and PbBiO$_2$Cl NPs, indicating that the conversion efficiency of benzyl alcohol to benzaldehyde had a positive correlation with the concentration of OVs under light irradiation. Moreover, to distinguish the effect of surface area, we further determined their specific activity, calculated as the mass activity normalized to the surface area. The specific activity of PbBiO$_2$Cl UBs still has 1.4-fold enha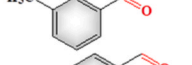ncement than PbBiO$_2$Cl NPs (Fig. S8), demonstrating the contribution of hollow bowl-shaped structure with ultrathin-shelled topologies, which facilitates charge separation and enhances light-harvesting. The further enhancement of specific activity for R$_{OV}$-PbBiO$_2$Cl UBs and P$_{OV}$-PbBiO$_2$Cl UBs could be attributed to the presence of OVs, which promote charge separation and O$_2$ activation. Control experiments showed that both the photocatalyst and light were essential for the conversion of benzyl alcohol. In addition, the conversion efficiency underwent sluggishly with the decrease of O$_2$ content under identical conditions, demonstrating the critical role of

molecular oxygen in valorizing benzyl alcohol (Fig. 4b). The catalytic activity of R$_{OV}$-PbBiO$_2$Cl UBs sample is competitive with most of the other up-to-date materials reported previously (Table S1). Besides, we also examined the influence of solvents on the photocatalytic activity, including acetonitrile, benzotrifluoride and n-hexane (Fig. 4c). It turned out that the conversion of benzyl alcohol was depending on the polarity of the solvent molecules, which could be attributed to competition absorption between the alcohol and the solvent molecules. A polar solvent is more easily adsorbed on the catalyst surface, preventing the adsorption of benzyl alcohol and thereby decreasing the conversion rate of benzyl alcohol oxidation [40]. Besides, the negligible activity decay and maintained crystal structure of the R$_{OV}$-PbBiO$_2$Cl UBs after four successive cycles collaboratively suggested that the photostability was favorable (Fig. 4d and Fig. S9).

In addition, a series of aromatic alcohols with different substituents were also examined to verify the applicability. As shown in Table 1, R$_{OV}$-PbBiO$_2$Cl UBs maintain a high efficiency in the selective transformation of aromatic alcohols no matter the substituent was electron-

Table 1
Photocatalytic aerobic oxidation of various aromatic alcohols with R_{OV}-PbBiO$_2$Cl UBs as catalyst.

Entry	Substrate	Product	Con. [%]	Sel. [%]
1			94	99
2			90	95
3			95	99
4			88	99
5			94	99
6			100	99
7			89	93
8			90	99

withdrawing or electron-donating. Nevertheless, compared with p-CH$_3$ and p-Cl substituted benzyl alcohol, the conversion and selectivity of benzyl alcohol substituted with m-CH$_3$ and m-Cl have a slight decrease. To gain more insights into benzyl alcohol conversion process, in situ Fourier transform infrared spectroscopy (FTIR) experiments were carried out (Fig. 4e). The peaks at 1374 cm^{-1} and 1457 cm^{-1} can be ascribed to the stretching vibration of O-H and the deformation vibration of C-H in benzyl alcohol, respectively [41,42]. After introducing light irradiation, a new peak at 1704 cm^{-1} was observed during the benzyl alcohol conversion process, which belonged to the (C=O) carbonyl stretch mode of benzaldehyde [43,44]. The gradually increased intensity of IR peaks over time indicated that benzyl alcohol was continuously adsorbed and converted into benzaldehyde.

3.3. Possible reaction mechanism

To disclose the role of different active radicals in the selective oxidation of aromatic alcohols into aldehydes, trapping experiments were conducted through casting various scavengers to the photoreaction system. As shown in Fig. 5a, the presence of scavengers for h$^+$ (TEOA), carbon centered radical (•C, BHT) and •O$_2^-$ (p-BQ) lead to a significant decrease in conversion rate, while the NaN$_3$ (^{1}O$_2$ scavenger), CCl$_4$ (e$^-$ scavenger) and IPA (•OH scavenger) shows a negligible effect for benzyl alcohol conversion, demonstrating that •O$_2^-$, h$^+$ and •C play an imperative role during the selective valorization of benzyl alcohol. These results were consistent with the formation of cation radical complex through hole oxidation in the •O$_2^-$ involved mechanism [40,45]. Therefore, the activation of O$_2$ and initial oxidation of benzyl alcohol into benzyl-type carbon-centered radicals are two crucial steps in the oxidation of benzyl alcohol into benzaldehyde. To verify the enhancement of the O$_2$ activation induced by the fabricating hollow

bowl-shaped structure with ultrathin-shelled topologies and abundant oxygen vacancies, we employed EPR spectra with DMPO as spin-trapping agent to study the active species generation by the four PbBiO$_2$Cl samples. As shown in Fig. 5b, the characteristic EPR signals corresponding to •O$_2^-$ were observed after light irradiation for 5 min, confirming the generation of •O$_2^-$. Additionally, the nitroxide-like radicals, formed through the cleavage of the N-C bond and ring opening of the DMPO-•O$_2^-$ adduct [46,47], were also detected by using DMPO as the trapping reagent in the benzyl alcohol n-hexane solution (Fig. 5c), further demonstrating the in-situ formation of •O$_2^-$. The gradually intensified •O$_2^-$ and nitroxide-like radical signals indicated that R_{OV}-PbBiO$_2$Cl UBs had a superior ability for O$_2$ activation to •O$_2^-$ compared to the P$_{OV}$-PbBiO$_2$Cl UBs, PbBiO$_2$Cl UBs and PbBiO$_2$Cl NPs, which can be attributed to the cooperation effect of rich oxygen vacancies and ultrathin bowl-shaped structure.

To further explore the origin of significantly boosted benzyl alcohol oxidation performance, the charge separation and transportation behaviors were systematically investigated. The photogenerated charge carrier dynamics of the PbBiO$_2$Cl samples are surveyed by time-resolved fluorescence emission decay spectra (Fig. 5d). The average lifetime has been extended from 4.01 ns (PbBiO$_2$Cl NPs) to 7.64 ns (PbBiO$_2$Cl UBs), demonstrating the contribution of hollow bowl-shaped structure with ultrathin-shelled topologies, which promoted charge separation by reducing diffusion resistance and boosted light-harvesting through extended light scattering. The further increase in fluorescence lifetime of the R_{OV}-PbBiO$_2$Cl UBs (16.39 ns) and P$_{OV}$-PbBiO$_2$Cl UBs (12.51 ns) unravels that the surface oxygen vacancies can actually prolong the lifetime of photogenerated carriers [48,49]. Moreover, as demonstrated by instantaneous photocurrent response in Fig. 5e, the R_{OV}-PbBiO$_2$Cl UBs show substantially increased current density relative to P$_{OV}$-PbBiO$_2$Cl UBs, PbBiO$_2$Cl UBs and PbBiO$_2$Cl NPs, further supporting that
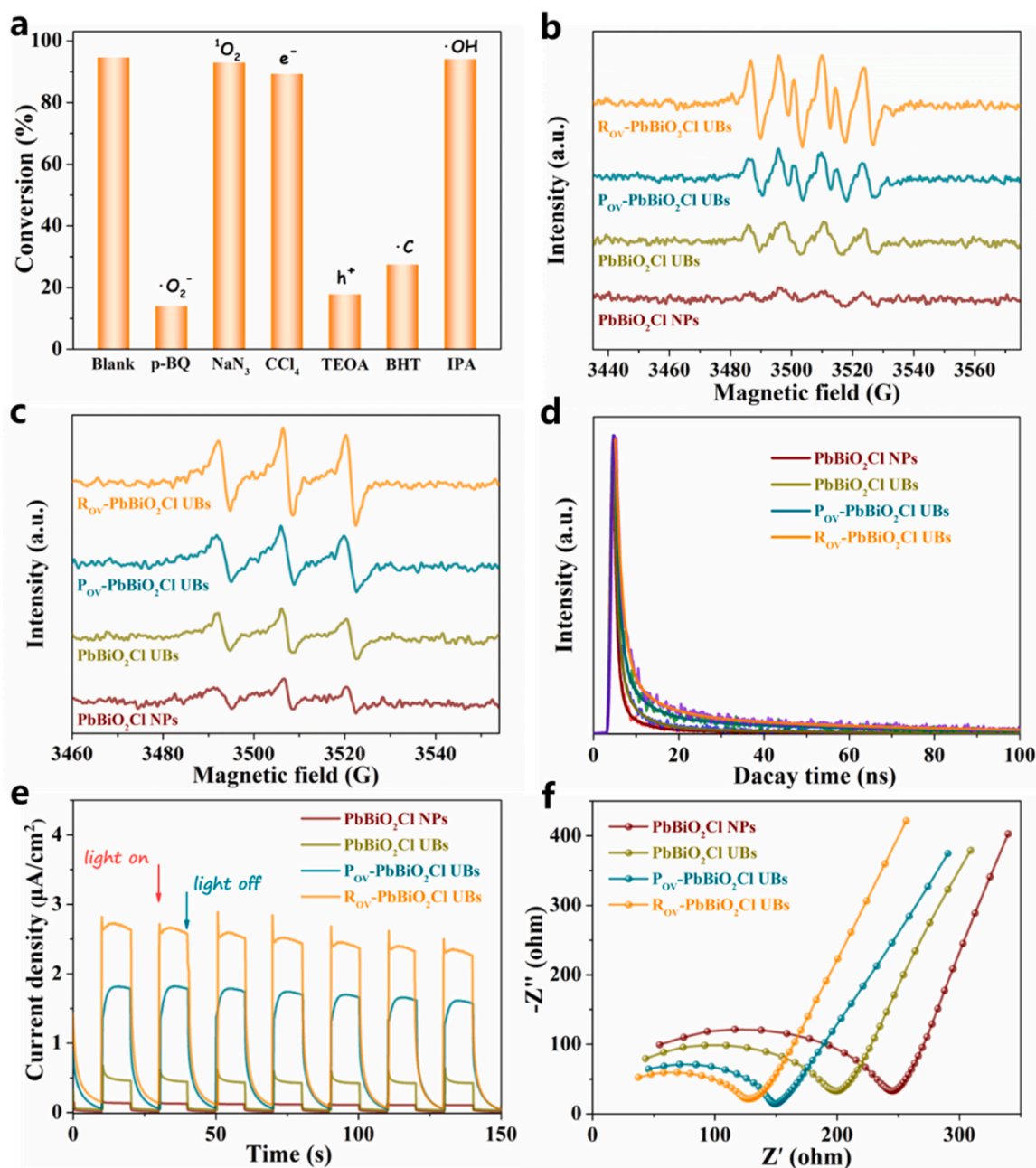
Fig. 5. (a) The reactive species trapping tests over R$_{OV}$-PbBiO$_2$Cl UBs with various scavengers. EPR detection of in situ formed (b) •O$_2^-$ in the presence of DMPO in methanol and (c) nitroxide-like radical in presence of DMPO in benzyl alcohol n-hexane solution under light irradiation. (d) Fluorescence emission decay spectra, (e) Transient photocurrent responses, (f) Electrochemical impedance spectra of the PbBiO$_2$Cl NPs and UBs.

ultrathin bowl-shaped configuration and abundant oxygen vacancies significantly facilitate the charge separation. Additionally, the Nyquist diagram suggests the smallest charge transfer resistance at the interface of R$_{OV}$-PbBiO$_2$Cl UBs, aligning well with the above fluorescence decay and photocurrent results (Fig. 5f) [50]. The multiple spectral results manifest that the fabrication of ultrathin bowl-shaped scaffolds and the introduction of OVs can cooperatively boost the charge separation efficiency in PbBiO$_2$Cl materials, rendering enhanced O$_2$-involved organic transformations.

To obtain a comprehensive understanding of the defect sites on the PbBiO$_2$Cl surface in the development of the charge carriers during O$_2$ activation process at atomic-level, the chemical interactions with O$_2$ on pristine PbBiO$_2$Cl slab and PbBiO$_2$Cl with OV slab were investigated. The O$_2$ adsorption energy on PbBiO$_2$Cl with OV slab was − 2.56 eV,

significantly lower than that on pristine PbBiO$_2$Cl slab (− 0.16 eV). Additionally, the bond length of O-O is considerably stretched from 1.24 Å to 1.45 Å, suggesting that O-O bonds are weakened in PbBiO$_2$Cl with OV slab. As shown in Fig. 6, the charge difference distribution and electron localization function (ELF) unambiguously uncover the existence of strong interfacial covalent bonds between molecular oxygen and OVs of PbBiO$_2$Cl, which can act as atomic-level electron transfer highway, and facilitates speedy and high flux electron exchange and transfer between OVs of PbBiO$_2$Cl and O$_2$. Moreover, the total charge (Δq) of O$_2$ increased from − 0.041 e (pristine PbBiO$_2$Cl) to − 1.670 e (PbBiO$_2$Cl with OV), further demonstrating that the O$_2$ molecule in defective PbBiO$_2$Cl acquired more electrons than in pristine PbBiO$_2$Cl, becoming effectively activated by speedy electron transfer processes and thus significantly promoting O$_2$-involved organic conversion.
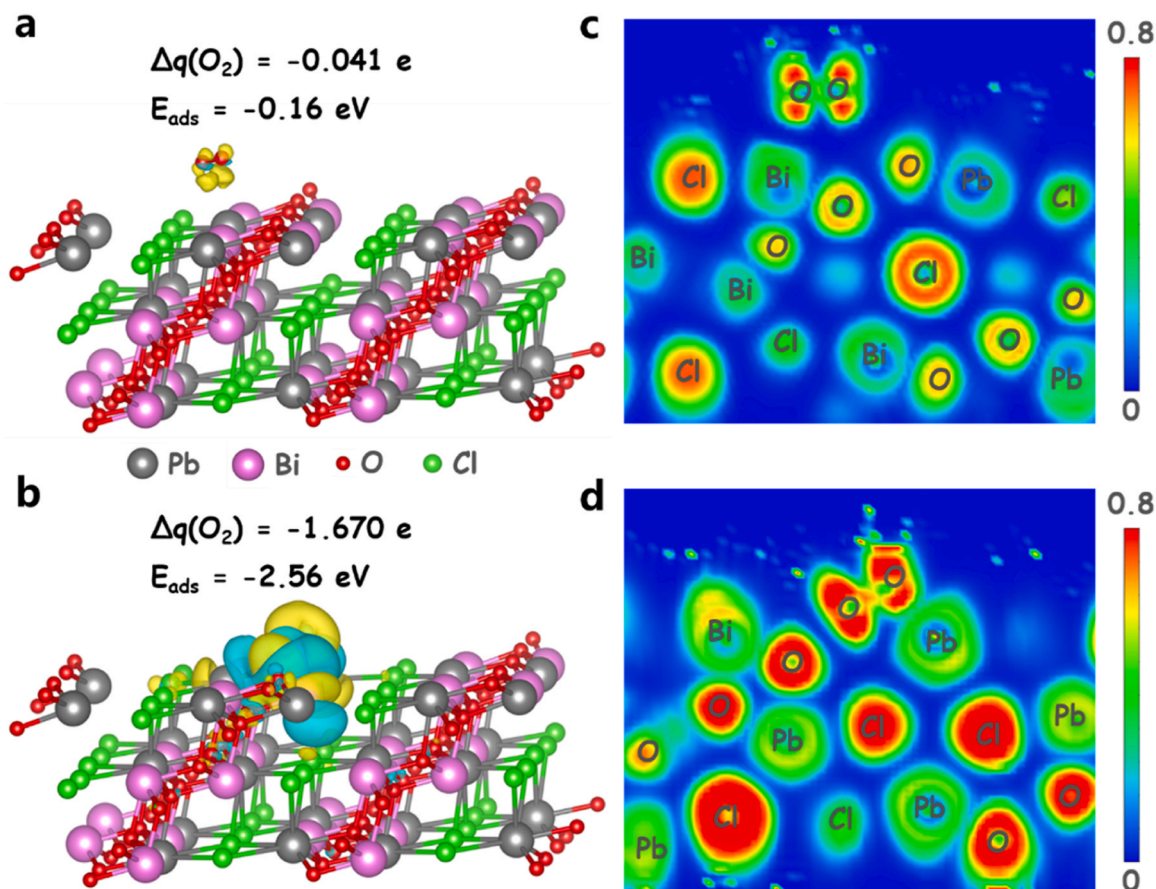
Fig. 6. Charge difference density of O_2 adsorbed on (a) pristine $PbBiO_2Cl$ and (b) $PbBiO_2Cl$ with OV (charge accumulation is in blue and depletion in yellow, isosurface set at 0.001e Å^{-3}). Electron localization function (ELF) of (c) pristine $PbBiO_2Cl$ and (d) $PbBiO_2Cl$ with OV.

Based on the above findings, a plausible reaction mechanism for elevated photocatalytic oxidation of aromatic alcohols over R_{OV}-$PbBiO_2Cl$ UBs was proposed. Firstly, the bowl-shaped scaffolds with ultrathin-shelled topologies endow the $PbBiO_2Cl$ with promoted charge separation and boosted light-harvesting. Meanwhile, OVs as trap states further upgrade electron and hole separation on the surface. Additionally, the presence of OVs gives rise to strong interfacial covalent bonds between molecular oxygen and OVs, which can serve as atomic-level electron transfer highway and benefits the electrons reduce O_2 into active intermediates ($\bullet O_2^-$) and the holes abstract electrons from the aromatic alcohols to yield alcohol cation radicals [51,52]. Finally, the obtained $\bullet O_2^-$ would abstract H from alcohol cation radicals to form the corresponding aldehydes.

4. Conclusion

In conclusion, ultrathin bowl-shaped $PbBiO_2Cl$ with tunable oxygen vacancy concentrations were initially prepared via a combined IL/W microemulsion approach and in-situ reduction method. The 3D bowl-shaped scaffolds with ultrathin shells effectively inhibit bulk recombination of electron-hole pairs owing to the reduced carrier diffusion resistance. The introduction of OVs on the surface of $PbBiO_2Cl$ not only extends the photo-absorption and boosts charge separation, but also generates abundant localized electrons and affords strong interfacial covalent bonds between molecular oxygen and OVs of $PbBiO_2Cl$, which can act as atomic-level electron transfer highway and effectively promote the molecular oxygen adsorption and activation. As a result, the R_{OV}-$PbBiO_2Cl$ UBs showed remarkably improved catalytic efficiency for aerobic oxidation of aromatic alcohols to aldehydes (Con. 94 %, Sel. **>** 99 %), which is 5.2 folds higher than that of $PbBiO_2Cl$ NPs. This work is

expected to inspire the design of more state-of-the-art systems based on ultrathin bowl-shaped photosynthetic scaffolds and defect engineering.

CRediT authorship contribution statement

Danjun Mao: Investigation, Conceptualization, Data curation, Funding acquisition, Methodology, Visualization, Writing – original draft. **Tong Li:** Data curation, Formal analysis, Investigation, Methodology, Validation. **Huan He:** Formal analysis, Funding acquisition, Methodology, Resources, Writing – review & editing. **Shuxue Yang:** Data curation, Methodology, Software. **Shaogui Yang:** Formal analysis, Supervision. **Cheng Sun:** Conceptualization, Supervision, Writing – review & editing. **Shourong Zheng:** Formal analysis, Methodology, Resources, Supervision. **Zhifeng Jiang:** Investigation, Data curation, Formal analysis. **Zhaoyi Xu:** Formal analysis, Funding acquisition, Methodology, Resources, Writing – review & editing. **Po Keung Wong:** Formal analysis, Methodology, Resources, Supervision. **Xiaolei Qu:** Formal analysis, Funding acquisition, Methodology, Resources, Writing – review & editing.

Declaration of Competing Interest

The authors declare that they have no known competing financial interests or personal relationships that could have appeared to influence the work reported in this paper.

Data availability

Data will be made available on request.

Acknowledgements

Appendix A. Supporting information

Supplementary data associated with this article can be found in the online version at doi:10.1016/j.apcatb.2023.123239.

References

[1] M.Y. Qi, M. Conte, M. Anpo, Z.R. Tang, Y.J. Xu, Cooperative coupling of oxidative organic synthesis and hydrogen production over semiconductor-based photocatalysts, Chem. Rev. 121 (2021) 13051–13085, https://doi.org/10.1021/acs.chemrev.1c00197.

[2] L.Q. Xiong, J.W. Tang, Strategies and challenges on selectivity of photocatalytic oxidation of organic substances, Adv. Energy Mater. 11 (2021), 2003216, https://doi.org/10.1002/aenm.202003216.

[3] C.Y. Toe, C. Tsounis, J.J. Zhang, H. Masood, D. Gunawan, J. Scott, R. Amal, Advancing photoreforming of organics: highlights on photocatalyst and system designs for selective oxidation reactions, Energy Environ. Sci. 14 (2021) 1140–1175, https://doi.org/10.1039/D0EE03116J.

[4] L.T. Xu, Z.F. Huang, M. Yang, J.C. Wu, W. Chen, Y.D. Wu, Y.P. Pan, Y.X. Lu, Y.Q. Zou, S.Y. Wang, Salting-out aldehyde from the electrooxidation of alcohols with 100% selectivity, Angew. Chem. Int. Ed. 61 (2022), e202210123, https://doi.org/10.1002/anie.202210123.

[5] G.L. Lu, F. Chu, X.B. Huang, Y.Q. Li, K.Y. Liang, G. Wang, Recent advances in metal-organic frameworks-based materials for photocatalytic selective oxidation, Coord. Chem. Rev. 450 (2022), 214240, https://doi.org/10.1016/j.ccr.2021.214240.

[6] Q. Wang, L.F. Chen, S.L. Guan, X. Zhang, B. Wang, X.Z. Cao, Z. Yu, Y.F. He, D.G. Evans, J.T. Feng, D.Q. Li, Ultrathin and vacancy-rich CoAl-layered double hydroxide/graphite oxide catalysts: promotional effect of cobalt vacancies and oxygen vacancies in alcohol oxidation, ACS Catal. 8 (2018) 3104–3115, https://doi.org/10.1021/acscatal.7b03655.

[7] Z.J. Zhu, H.W. Huang, L.Z. Liu, F. Chen, N. Tian, Y.H. Zhang, H. Yu, Chemically bonded α-Fe$_2$O$_3$/Bi$_4$MO$_8$Cl Dot-on-Plate Z-scheme junction with strong internal electric field for selective photooxidation of aromatic alcohols, Angew. Chem. Int. Ed. 61 (2022), e202203519, https://doi.org/10.1002/anie.202203519.

[8] Z.F. Yang, X.N. Xia, W.W. Yang, L.L. Wang, Y.T. Liu, Photothermal effect and continuous hot electrons injection synergistically induced enhanced molecular oxygen activation for efficient selective oxidation of benzyl alcohol over plasmonic W$_{18}$O$_{49}$/ZnIn$_2$S$_4$ photocatalyst, Appl. Catal. B Environ. 299 (2021), 120675, https://doi.org/10.1016/j.apcatb.2021.120675.

[9] X.S. Sun, X.D. Zhang, Yi Xie, Surface defects in two-dimensional photocatalysts for efficient organic synthesis, Matter 2 (2020) 842–861, https://doi.org/10.1016/j.matt.2020.02.006.

[10] J.H. Zou, Z.T. Wang, W. Guo, B.B. Guo, Y. Yu, L. Wu, Photocatalytic selective oxidation of benzyl alcohol over ZnTi-LDH: the effect of surface OH groups, Appl. Catal. B Environ. 260 (2020), 118185, https://doi.org/10.1016/j.apcatb.2019.118185.

[11] E. Tiburcio, R. Greco, M. Mon, J. Soberanas, J. Soria, M. Haro, J. Garrido, J. Meseguer, C. Marini, M. Boronat, D. Armentano, A. Pérez, E. Pardo, Soluble/MOF-supported palladium single atoms catalyze the ligand-, additive-, and solvent-free aerobic oxidation of benzyl alcohols to benzoic acids, J. Am. Chem. Soc. 143 (2021) 2581–2592, https://doi.org/10.1021/jacs.0c12367.

[12] T. Xia, W.B. Gong, Y.H. Chen, M.L. Duan, J. Ma, X.F. Cui, Y.T. Dai, C. Gao, Y.J. Xiong, Sunlight-driven highly selective catalytic oxidation of 5-hydroxymethylfurfural towards tunable products, Angew. Chem. Int. Ed. 61 (2022), e202204225, https://doi.org/10.1002/anie.202204225.

[13] M. Zhang, Z.H. Yu, J. Xiong, R. Zhang, X.Z. Liu, X.B. Lu, One-step hydrothermal synthesis of Cd$_x$In$_y$S$_{(x+1.5y)}$ for photocatalytic oxidation of biomass-derived 5-hydroxymethylfurfural to 2, 5-diformylfuran under ambient conditions, Appl. Catal. B Environ. 300 (2022), 120738, https://doi.org/10.1016/j.apcatb.2021.120738.

[14] D.J. Mao, S.X. Yang, Y. Hu, H. He, S.G. Yang, S.R. Zheng, C. Sun, Z.F. Jiang, X.L. Qu, P.K. Wong, Efficient CO$_2$ photoreduction triggered by oxygen vacancies in ultrafine Bi$_5$O$_7$Br nanowires, Appl. Catal. B Environ. 321 (2023), 122031, https://doi.org/10.1016/j.apcatb.2022.122031.

[15] Z.L. Tian, C. Han, Y. Zhao, W.R. Dai, X. Lian, Y.N. Wang, Y. Zheng, Y. Shi, X. Pan, Z.C. Huang, H.X. Li, W. Chen, Efficient photocatalytic hydrogen peroxide generation coupled with selective benzylamine oxidation over defective ZrS$_3$ nanobelts, Nat. Commun. 12 (2021) 2039, https://doi.org/10.1038/s41467-021-22394-8.

[16] Y.X. Li, M.M. Wen, Y. Wang, G. Tian, C.Y. Wang, J.C. Zhao, Plasmonic hot electrons from oxygen vacancies for infrared light-driven catalytic CO$_2$ reduction on Bi$_2$O$_{3-x}$, Angew. Chem. Int. Ed. 60 (2021) 910–916, https://doi.org/10.1002/anie.202010156.

[17] D.J. Mao, Y. Hu, S.X. Yang, J.L. Liang, H. He, S.G. Yang, Z.Y. Xu, C. Sun, S.R. Zheng, Z.F. Jiang, X.L. Qu, C.S. Lee, Oxygen-vacancy-induced charge localization and atomic site activation in ultrathin Bi$_4$O$_5$Br$_2$ nanotubes for boosted CO$_2$ photoreduction, Chem. Eng. J. 452 (2023), 139304, https://doi.org/10.1016/j.cej.2022.139304.

[18] C.L. Mao, H.G. Cheng, H. Tian, H. Li, W.J. Xiao, H. Xu, J.C. Zhao, L.Z. Zhang, Visible light driven selective oxidation of amines to imines with BiOCl: does oxygen vacancy concentration matter? Appl. Catal. B Environ. 228 (2018) 87–96, https://doi.org/10.1016/j.apcatb.2018.01.018.

[19] H. Li, F. Qin, Z.P. Yang, X.M. Cui, J.F. Wang, L.Z. Zhang, New reaction pathway induced by plasmon for selective benzyl alcohol oxidation on BiOCl possessing oxygen vacancies, J. Am. Chem. Soc. 139 (2017) 3513–3521, https://doi.org/10.1021/jacs.6b12850.

[20] Y.T. Dai, P.J. Ren, Y.R. Li, D. Lv, Y. Shen, Y. Li, H. Niemantsverdriet, F. Besenbacher, H.W. Xiang, W.C. Hao, N. Lock, X.D. Wen, J.P. Lewis, R. Su, Solid base Bi$_{24}$O$_{31}$Br$_{10}$(OH)$_\delta$ with active lattice oxygen for the efficient photo-oxidation of primary alcohols to aldehydes, Angew. Chem. Int. Ed. 58 (2019) 6265–6270, https://doi.org/10.1002/anie.201900773.

[21] S. Wei, H.X. Zhong, H.T. Wang, Y.J. Song, C.M. Jia, M. Anpo, L. Wu, Oxygen vacancy enhanced visible light photocatalytic selective oxidation of benzylamine over ultrathin Pd/BiOCl nanosheets, Appl. Catal. B Environ. 305 (2022), 121032, https://doi.org/10.1016/j.apcatb.2021.121032.

[22] X. Xiao, C.X. Zheng, M.L. Lu, L. Zhang, F. Liu, X.X. Zuo, J.M. Nan, Deficient Bi$_{24}$O$_{31}$Br$_{10}$ as a highly efficient photocatalyst for selective oxidation of benzyl alcohol into benzaldehyde under blue LED irradiation, Appl. Catal. B Environ. 228 (2018) 142–151, https://doi.org/10.1016/j.apcatb.2018.01.076.

[23] J. Liang, H.R. Kou, S.J. Ding, Complex hollow bowl-like nanostructures: synthesis, application, and perspective, Adv. Funct. Mater. 31 (2021), 2007801, https://doi.org/10.1002/adfm.202007801.

[24] L. Yuan, C.Q. Zhang, J. Wang, C. Liu, C.Z. Yu, Mesoporous resin nanobowls with optimized donor–acceptor conjugation for highly efficient photocatalytic hydrogen peroxide production, Nano Res. 14 (2021) 3267–3273, https://doi.org/10.1007/s12274-021-3517-6.

[25] D.J. Mao, J.L. Yuan, X.L. Qu, C. Sun, S.G. Yang, H. He, Size tunable Bi$_3$O$_4$Br hierarchical hollow spheres assembled with {001}-facets exposed nanosheets for robust photocatalysis against phenolic pollutants, J. Catal. 369 (2019) 209–221, https://doi.org/10.1016/j.jcat.2018.11.016.

[26] D.J. Mao, S.S. Ding, L.J. Meng, Y.X. Dai, C. Sun, S.G. Yang, H. He, One-pot microemulsion-mediated synthesis of Bi-rich Bi$_4$O$_5$Br$_2$ with controllable morphologies and excellent visible-light photocatalytic removal of pollutants, Appl. Catal. B Environ. 207 (2017) 153–165, https://doi.org/10.1016/j.apcatb.2017.02.010.

[27] H.J. Yu, J.Y. Li, Y.H. Zhang, S.Q. Yang, K.L. Han, F. Dong, T.Y. Ma, H.W. Huang, Three-in-one oxygen vacancies: whole visible-spectrum absorption, efficient charge separation, and surface site activation for robust CO$_2$ photoreduction, Angew. Chem. Int. Ed. 58 (2019) 3880–3884, https://doi.org/10.1002/anie.201813967.

[28] F. Chen, Z.Y. Ma, L.Q. Ye, T.Y. Ma, T.R. Zhang, Y.H. Zhang, H.W. Huang, Macroscopic spontaneous polarization and surface oxygen vacancies collaboratively boosting CO$_2$ photoreduction on BiOIO$_3$ single crystals, Adv. Mater. 32 (2020), 1908350, https://doi.org/10.1002/adma.201908350.

[29] Z. Wu, P.Y. Zhang, S.P. Rong, J.B. Jia, Creating water-resistant oxygen vacancies in δ-MnO$_2$ by chlorine introduction for catalytic ozone decomposition at ambient temperature, Appl. Catal. B: Environ. 335 (2023), 122900, https://doi.org/10.1016/j.apcatb.2023.122900.

[30] Y. Zhang, J. Di, X. Qian, M.X. Ji, Z.Q. Tian, L.Q. Ye, J.Z. Zhao, S. Yin, H.M. Li, J.X. Xia, Oxygen vacancies in Bi$_2$Sn$_2$O$_7$ quantum dots to trigger efficient photocatalytic nitrogen reduction, Appl. Catal. B Environ. 276 (2020), 119156, https://doi.org/10.1016/j.apcatb.2020.119156.

[31] X.Z. Zhao, Y.G. Xia, H.P. Li, X. Wang, J. Wei, X.L. Jiao, D.R. Chen, Oxygen vacancy dependent photocatalytic CO$_2$ reduction activity in liquid-exfoliated atomically thin BiOCl nanosheets, Appl. Catal. B Environ. 297 (2021), 120426, https://doi.org/10.1016/j.apcatb.2021.120426.

[32] X.J. Tong, X. Cao, T. Han, W.C. Cheong, R. Lin, Z. Chen, D.S. Wang, C. Chen, Q. Peng, Y.D. Li, Convenient fabrication of BiOBr ultrathin nanosheets with rich oxygen vacancies for photocatalytic selective oxidation of secondary amines, Nano Res. 12 (2019) 1625–1630, https://doi.org/10.1007/s12274-018-2404-x.

[33] D.N. Liu, D.Y. Chen, N.J. Li, Q.F. Xu, H. Li, J.H. He, J.M. Lu, Surface engineering of g-C$_3$N$_4$ by stacked BiOBr sheets rich in oxygen vacancies for boosting photocatalytic performance, Angew. Chem. Int. Ed. 59 (2020) 4519–4524, https://doi.org/10.1002/anie.201914949.

[34] C. Li, H. Jang, M.G. Kim, L.Q. Hou, X.E. Liu, J. Cho, Ru-incorporated oxygen-vacancy-enriched MoO$_2$ electrocatalysts for hydrogen evolution reaction, Appl. Catal. B Environ. 307 (2022), 121204, https://doi.org/10.1016/j.apcatb.2022.121204.

[35] L.Z. Liu, H.W. Huang, F. Chen, H.J. Yu, N. Tian, Y.H. Zhang, T.R. Zhang, Cooperation of oxygen vacancies and 2D ultrathin structure promoting CO$_2$ photoreduction performance of Bi$_4$Ti$_3$O$_{12}$, Sci. Bull. 65 (2020) 934–943, https://doi.org/10.1016/j.scib.2020.02.019.

[36] Y.B. Shi, G.M. Zhan, H. Li, X.B. Wang, X.F. Liu, L.J. Shi, K. Wei, C.C. Ling, Z.L. Li, H. Wang, C.L. Mao, X. Liu, L.Z. Zhang, Simultaneous manipulation of bulk excitons

and surface defects for ultrastable and highly selective CO₂ photoreduction, Adv. Mater. 33 (2021), 2100143, https://doi.org/10.1002/adma.202100143.

[37] Y.P. Zhang, T. Song, X. Zhou, Y. Yang, Oxygen-vacancy-boosted visible light driven photocatalytic oxidative dehydrogenation of saturated N-heterocycles over Nb₂O₅ nanorods, Appl. Catal. B Environ. 316 (2022), 121622, https://doi.org/10.1016/j.apcatb.2022.121622.

[38] Y.S. Mao, P.F. Wang, L.N. Li, Z.W. Chen, H.T. Wang, Y. Li, S.H. Zhan, Unravelling the synergy between oxygen vacancies and oxygen substitution in BiO₂₋ₓ for efficient molecular-oxygen activation, Angew. Chem. Int. Ed. 59 (2020) 3685–3690, https://doi.org/10.1002/anie.201914001.

[39] R.J. Gao, L. Pan, Z.W. Li, C.X. Shi, Y.D. Yao, X.W. Zhang, J.J. Zou, Engineering facets and oxygen vacancies over hematite single crystal for intensified electrocatalytic H₂O₂ production, Adv. Funct. Mater. 30 (2020), 1910539, https://doi.org/10.1002/adfm.201910539.

[40] X.L. Bao, H.L. Li, Z.Y. Wang, F.X. Tong, M. Liu, Z.K. Zheng, P. Wang, H.F. Cheng, Y. Y. Liu, Y. Dai, Y.C. Fan, Z.Y. Li, B.B. Huang, TiO₂/Ti₃C₂ as an efficient photocatalyst for selective oxidation of benzyl alcohol to benzaldehyde, Appl. Catal. B Environ. 286 (2021), 119885, https://doi.org/10.1016/j.apcatb.2021.119885.

[41] D.Y. Feng, Y.B. Dong, L.L. Zhang, X. Ge, W. Zhang, S. Dai, Z.A. Qiao, Holey Lamellar high-entropy oxide as an ultra-high-activity heterogeneous catalyst for solvent-free aerobic oxidation of benzyl, Alcohol, Angew. Chem. Int. Ed. 59 (2020) 19503–19509, https://doi.org/10.1002/anie.202004892.

[42] Z.Y. Zhou, Y.N. Xie, W.Z. Zhu, H.Y. Zhao, N.J. Yang, G.H. Zhao, Selective photoelectrocatalytic tuning of benzyl alcohol to benzaldehyde for enhanced hydrogen production, Appl. Catal. B Environ. 286 (2021), 119868, https://doi.org/10.1016/j.apcatb.2020.119868.

[43] Z.L. Sun, X.L. Yang, X.F. Yu, L.H. Xia, Y.H. Peng, Z. Li, Y. Zhang, J.B. Cheng, K. S. Zhang, J.Q. Yu, Surface oxygen vacancies of Pd/Bi₂MoO₆₋ₓ acts as "Electron Bridge" to promote photocatalytic selective oxidation of alcohol, Appl. Catal. B Environ. 285 (2021), 119790, https://doi.org/10.1016/j.apcatb.2020.119790.

[44] L. Luo, Z.J. Wang, X. Xiang, D.P. Yan, J.H. Ye, Selective activation of benzyl alcohol coupled with photoelectrochemical water oxidation via a radical relay strategy, ACS Catal. 10 (2020) 4906–4913, https://doi.org/10.1021/acscatal.0c00660.

[45] J.G. Wang, H. Liang, C. Zhang, B. Jin, Y. Men, Bi₂WO₆₋ₓ nanosheets with tunable Bi quantum dots and oxygen vacancies for photocatalytic selective oxidation of alcohols, Appl. Catal. B Environ. 256 (2019), 117874, https://doi.org/10.1016/j.apcatb.2019.117874.

[46] H.W. Huang, C. Zhou, X.C. Jiao, H.F. Yuan, J.W. Zhao, C.Q. He, J. Hofkens, M.B. J. Roeffaers, J.L. Long, J.A. Steele, Subsurface defect engineering in single-unit-cell Bi₂WO₆ monolayers boosts solar-driven photocatalytic performance, ACS Catal. 10 (2020) 1439–1443, https://doi.org/10.1021/acscatal.9b04789.

[47] E.Z. Lin, R. Huang, J. Wu, Z.H. Kang, K.H. Ke, N. Qin, D.H. Bao, Recyclable CoFe₂O₄ modified BiOCl hierarchical microspheres utilizing photo, photothermal and mechanical energy for organic pollutant degradation, Nano Energy 89 (2021), 106403, https://doi.org/10.1016/j.nanoen.2021.106403.

[48] S.G. Li, F. Chen, S.Q. Chu, Z.Y. Zhang, J.D. Huang, S.Y. Wang, Y.B. Feng, Z. Y. Wang, H.W. Huang, Synergy-compensation effect of ferroelectric polarization and cationic vacancy collaboratively promoting CO₂ Photoreduction, Small 19 (2023), 2203559, https://doi.org/10.1002/smll.202203559.

[49] T. Song, C. Wang, Y.P. Zhang, X.L. Shi, Y.F. Li, Y. Yang, Visible-light-induced oxidative alkene difunctionalization to access α-sulfonyloxy ketones catalyzed by oxygen-vacancy-rich Nb₂O₅, Appl. Catal. B Environ. 304 (2022), 120964, https://doi.org/10.1016/j.apcatb.2021.120964.

[50] Z. Xu, Y.J. Wu, X. Wang, Q.Y. Ji, T.Z. Li, H. He, H.O. Song, S.G. Yang, S.Y. Li, S. C. Yan, L.M. Zhang, Z.G. Zou, Identifying the role of oxygen vacancy on cobalt-based perovskites towards peroxymonosulfate activation for efficient iohexol degradation, Appl. Catal. B Environ. 319 (2022), 120901, https://doi.org/10.1016/j.apcatb.2022.121901.

[51] C. Xu, F. Yang, B.J. Deng, Y. Zhuang, D.Y. Li, B.C. Liu, W. Yang, Y.F. Li, Ti₃C₂/TiO₂ nanowires with excellent photocatalytic performance for selective oxidation of aromatic alcohols to aldehydes, J. Catal. 383 (2020) 1–12, https://doi.org/10.1016/j.jcat.2020.01.001.

[52] P.L. Wang, X.Y. Li, S.Y. Fan, Z.F. Yin, L. Wang, M.O. Tadé, S.M. Liu, Piezotronic effect and oxygen vacancies boosted photocatalysis C-N coupling of benzylamine, Nano Energy 83 (2021), 105831, https://doi.org/10.1016/j.nanoen.2021.105831.